

## Experimental and Numerical Studies of a Laboratory Fire Whirl

K. Hartl<sup>1</sup>, H. M. Blackburn<sup>2</sup> and A. J. Smits<sup>1</sup>

<sup>1</sup>Mechanical and Aerospace Engineering  
 Princeton University, NJ 08540, USA

<sup>2</sup>Department of Mechanical and Aerospace Engineering  
 Monash University, Victoria 3800, Australia

### Abstract

Results from a laboratory study of a fire whirl with dimethyl ether fuel are introduced and discussed in relation to fundamental and semi-empirical scaling results. The laboratory study also forms the basis for a stabilised direct numerical simulation (DNS) study of convection with Boussinesq buoyancy. A comparison of results suggests the basic simulation methodology holds promise but that a tighter characterisation of simulation and experimental boundary conditions will benefit future work.

### Introduction

Fire whirls are standing vortex structures that form under the combined action of buoyant forces and ambient vorticity. Rising accelerating air due to buoyant forces from flames on the ground drives the mass flow towards the base of the fire. In the presence of ambient vorticity, a vortex is formed over the fire due to the tilting and stretching of vorticity by buoyancy forces. Fire whirls are common in bush and wild fires, and may be a principal mechanism for advancing the fire line through spotting (figure 1 *a*).

Buoyancy and rotation of the flame are linked through conservation of angular momentum; buoyancy stretches the vortex core and consequently speeds up the core rotation [7]. Dimensional analysis reveals that the non-dimensional height of the fire whirl is a function only of the heat release rate and the circulation. Our experiments indicate that the height only depends on the circulation, independent of the heat release rate. This result is counter-intuitive, in that buoyancy stretches the vortex, which will tend to reduce turbulent mixing by enhancing stabilising rotation.

To investigate the same flow numerically, we employ a stabilised direct numerical simulation of the Navier–Stokes and temperature transport equations, coupled using the Boussinesq buoyancy approximation. The simulation approach allow us to independently control background circulation and buoyancy.

### Experimental setup

To study fire whirls in the laboratory, a burner with dimethyl ether (DME) as fuel is used as the fire source, and two offset plexiglass cylinder halves are used to control the ambient vorticity (figures 1 *b* and 2). The burner flame provides a constant source of buoyancy. Staggering the plexiglass cylinder halves around the burner imparts tangential velocity to the flow moving towards the burner, thus establishing a vortex flow.

The experimental rig is assembled from a DME burner 40 mm in diameter and two offset 900 mm long, 300 mm diameter semi-cylinders, as shown in figure 2. Heat release rate is controlled by adjusting the mass flow rate of DME; using its enthalpy of combustion (1460 kJ/mol) and the area of the burner we compute the heat generation per unit area  $q$ . Maximum heating rate in the experiments was 1.9 kW. Stereo particle image



Figure 1: (a) full scale (outback Australia, 2013) and (b) laboratory scale fire whirls.

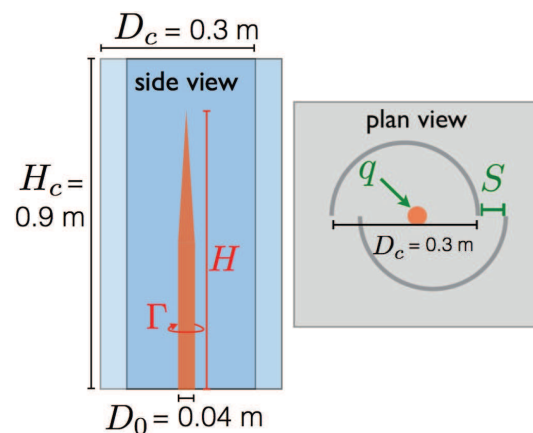


Figure 2: Diagram of experimental setup. Heat source  $q$  is a dimethyl ether flame.

velocimetry (PIV) is used to obtain velocity components from movements of fog particles in regions outside the flame. The circulation of flow near the flame,  $\Gamma$ , was assessed from the azimuthal velocity distribution, and whirl height  $H$  was assessed visually from flame luminosity. Inflow swirl was modified by varying gap size  $S$  between the two semi-cylinders, which in the experiments varied between 50 and 150 mm.

### Numerical methods

Simulation is carried out using a spectral element–Fourier method for the Navier–Stokes equations in cylindrical coordinates [2] with a coupled advection–diffusion solver for heat transport. Buoyancy is introduced using the Boussinesq approximation in which the flow is treated as incompressible, but buoyancy terms appear in the momentum equations treated in primitive ( $\mathbf{u}, p$ ) variables. Gravitational acceleration  $\mathbf{g}$  is aligned with

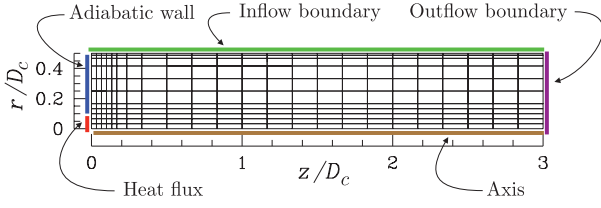


Figure 3: Spectral element mesh of the computational domain's meridional semiplane, with 253 spectral elements. Layout of boundary conditions is indicated. Gravitational body forces point in the negative axial ( $z$ ) direction, input heat flux occurs over the lowest two element boundaries at  $z = 0$ .

the axis of the cylindrical coordinate system. The set of equations for solution is then

$$\partial_t \mathbf{u} + \mathbf{u} \cdot \nabla \mathbf{u} = -\rho^{-1} \nabla p + \nu \nabla^2 \mathbf{u} - \beta \theta \mathbf{g}, \quad (1)$$

$$\partial_t \theta + \mathbf{u} \cdot \nabla \theta = \alpha \nabla^2 \theta, \quad (2)$$

$$\nabla \cdot \mathbf{u} = 0, \quad (3)$$

where  $\theta$  is absolute temperature difference relative to reference temperature  $\theta_{\text{ref}}$  (assumed to match air at standard conditions),  $\beta$  is the coefficient of thermal expansion; for a perfect gas  $\beta = 1/\theta_{\text{ref}}$ . The coefficients for diffusion of momentum and temperature are  $\nu$  and  $\alpha$  respectively; following convention we take  $\alpha = \nu/Pr$  and have used the Prandtl number  $Pr = 0.71$ , representing air at standard conditions. Axial, radial and azimuthal velocity components are represented by  $\mathbf{u} = (u, v, w)$ , respectively, while fluctuations of solution variables around their temporal mean values are given as  $(u', v', w', p', \theta')$

The set of equations above is integrated in time using backwards differencing and a time-split treatment [2]. Recognising that the flow will be under-resolved on the mesh shown in figure 3, we use a hyperviscosity approach to flow stabilisation, as outlined in [5]. The ratio of diffusion coefficients at the highest wavenumbers employed to the background values was 20:1. At the outflow of the domain, a robust set of boundary conditions is employed for velocity and pressure [3].

The computational domain (figure 3) had a length:diameter ratio of 3:1, the same as  $H_c/D_c$  for the experimental apparatus. Details of the computational mesh and allocation of boundary conditions are also shown in figure 3. The meridional semiplane was discretized using 253 spectral elements, each with 8th-order tensor product basis functions. Fourier expansions were employed in azimuth, with a total number of 32 Fourier modes or 64 planes of real data. Total number of independent mesh nodes was just over 1 million.

Instead of modelling a combustion process (since it is assumed that the coupling of buoyancy and swirl is the most important factor, rather than the detailed nature of the heat release mechanism), heat is input to the domain using flux (gradient) boundary conditions, over an area of the domain boundary scaled on  $D_0/D_c$  in the experiment. In what is possibly a more significant deviation from experimental conditions, uniform radial and swirl velocities were assumed over the entire outer radius of the domain. This is a reasonable assumption for entrainment by a turbulent non-swirling jet issuing from a wall [8], however, since details of the axial distributions of far-field velocities were not available from the experiment, it amounts to an educated guess. The ratio of swirl to radial velocity components on the inflow was assumed to be unity. The total amount of volumetric inflow was unknown, but was characterised approximately from near-field radial velocity values measured near the base of the

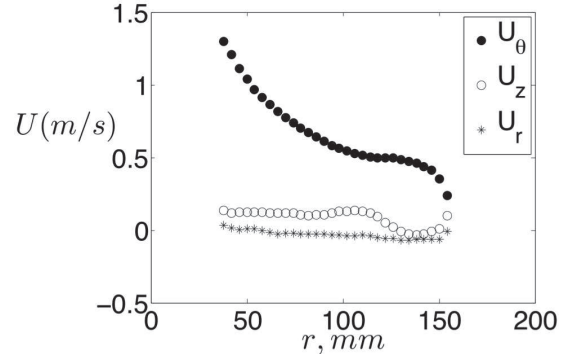


Figure 4: Experimental measurements showing radial distributions of mean velocity components at  $z/D_c = 0.9$  and  $S^* = S/D_0 = 0.16$  for the highest heat release rate of 1.9 kW,  $q^* = 0.95$ .

flame in the experiments (and is significantly greater than required by simple stoichiometry). The amount of heat flux over the lower wall was initially scaled based on an assumed 1 kW heat release rate, but eventually it was found necessary to employ 1% of this value in order to obtain stable simulations with the domain size and far-field boundary conditions employed. This means that there is likely to be a larger inflow:buoyancy ratio in the simulations than in the experiments. A far tighter characterisation of experimental boundary values and heat input distribution is required to support the computations, and these are in progress.

Unless otherwise stated, velocities in the simulation results are non-dimensionalised based on the assumed uniform far-field radial inflow velocity,  $U$ . The Reynolds number based on this and the domain length scale,  $D_c$ , was  $Re = UD_c/\nu = 27.7$ . While that may seem rather low, we note that the Reynolds number based on the peak mean axial velocity was  $Re = \langle \hat{u} \rangle D_c/\nu = 950$ .

## Experimental results

Figure 4 illustrates experimental measurements of mean velocities at the smallest gap width and heat release rate. Note that measurements do not extend inside the flame, and that the azimuthal velocity distribution approximates that for a free vortex (so the circulation is reasonably constant over much of the radius).

Under assumptions that the maximum density and temperature variations from background values (respectively  $\Delta \rho = \rho - \rho_0$  and  $\Delta T = T - T_0$ ) are nearly constant in ordinary fires, that the ratio of whirl diameter to burner diameter is a constant of order unity, and that the ratio of potential to thermal energy in the whirl is small, one finds from dimensional considerations that the whirl centreline speed and diameter are no longer functions of height. Again based on dimensional considerations, this suggests that the dimensionless flame height  $H^* = H/D_0$ , dimensionless swirl circulation  $\Gamma^* = \Gamma/D_0\sqrt{gD_0}$  and dimensionless heat release rate  $q^* = q/(C_{p0}\rho_0\Delta T D_0^2\sqrt{gD_0})$  are related through a universal function

$$H^* = f_1(\Gamma^*, q^*). \quad (4)$$

In the experiments, the circulation can be influenced by changing the dimensionless gap width  $S^* = S/D_0$ , and the heat release rate  $q$  is controlled by mass flow rate of DME. One expects relationships of the forms

$$\Gamma^* = f_2(S^*, q^*), \quad H^* = f_3(S^*, q^*), \quad (5)$$

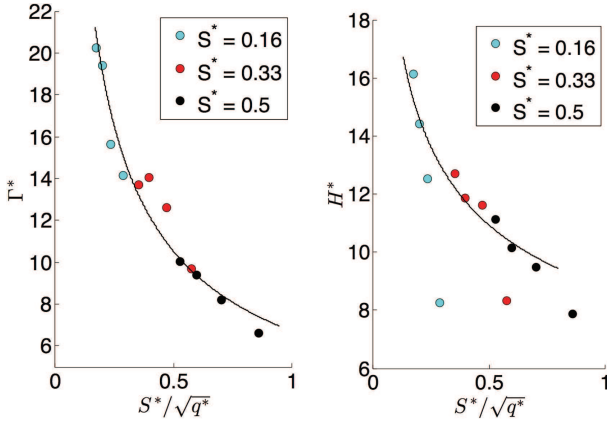


Figure 5: Dimensionless whirl circulation and height.

which are confirmed by the results given in figure 5 (if one ignores  $H^*$  values for the smallest heat release rate on the basis that the circulation was too small to affect whirl height). Power-law fits to the data of figure 5 provide

$$\Gamma^* = 6.6(S^*/\sqrt{q^*})^{-0.65}, \quad H^* = 8.7(S^*/\sqrt{q^*})^{-0.32}. \quad (6)$$

Substituting the first of these relationships into the second, one obtains

$$H^* = 3.4\sqrt{\Gamma^*}, \quad (7)$$

suggesting that the dimensionless whirl height is only a weak function of dimensionless heat release rate, at best. Similar power-law relationships relating  $H^*$  and  $\Gamma^*$  have been proposed by other groups [1, 6].

### Computational results

The computation was initiated in solid-body rotation and computed with a restriction to axisymmetry until an approximate steady state was reached, then projected to three dimensions and perturbed with white noise. After evolving to an approximate equilibrium, resolution was increased and then after further settling, when a new approximate statistical equilibrium was achieved, collection of statistics was initiated.

To illustrate the nature of the flow achieved by our stabilised DNS, we show in figure 6 a snapshot perspective view of isosurfaces of  $\theta$  (to indicate the buoyant plume) and an (negative-valued) isosurface of the vortex core measure  $\lambda_2$  [4], derived from the velocity gradient field, to indicate turbulent flow structures. As the plume rises, it becomes turbulent and also weaker through both diffusion and turbulent mixing. Evidently the turbulence has a significant amount of fine-scale structure considering the comparatively low nominal Reynolds number.

The distribution of  $U/\langle u \rangle$  along the axis of the domain is shown in figure 7. After an initial settling phase in which the axial velocity is approximately independent of elevation, the distribution exhibits a region where the inverse mean value rises linearly with distance, starting at a virtual origin near  $z/D_c = 0.25$ . The distribution of inverse temperature (not shown) displays similar behaviour. These scalings indicate that plume buoyancy is no longer significant above a certain elevation, and after a region of initial acceleration to a constant axial speed, the plume starts to behave similarly to turbulent jet carrying a passive scalar [9]. However, at lower elevations, the fact that  $\langle u \rangle/U$  initially becomes approximately independent of  $z$  is in line with the assumptions (and experimental observations) for fire whirls.

Radial distributions of mean flow velocities at two different elevations are shown in figure 8. At the lower elevation ( $z/D_c =$

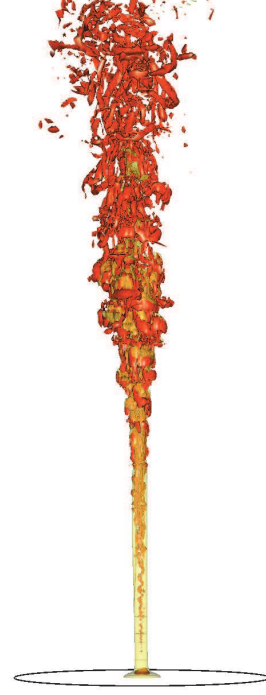


Figure 6: Snapshot perspective view of buoyant turbulent plume simulation. Yellow translucent isosurface for temperature  $\theta$ , red isosurface shows the vortex core measure  $\lambda_2$  [4].

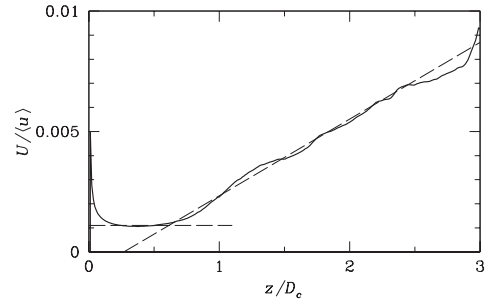


Figure 7: Distribution of inverse mean axial velocity along the plume axis.

0.1), the azimuthal velocity distribution resembles that for a Lamb–Oseen vortex, approaching solid-body rotation near the axis and a free vortex at larger radii. The axial velocity component in the near-axis region is by comparison very large. At the larger elevation ( $z/D_c = 0.9$ , the same value as for the experimental data of figure 4) the largest azimuthal flow speed occurs at mid radius but with a secondary peak closer to the axis. The axial velocity at this elevation shows a moderate reverse flow near the outer radius.

Two-dimensional spatial distributions of flow statistics are presented in figure 9 (statistics have been averaged in both time and azimuth). The mean scalar field and sectional streamlines shown in figure 9(a) suggest that the plume starts to spread more rapidly from around  $z/D_c \approx 0.3$  and also that there is a large (though slow) recirculation region trapped between the buoyant plume and the inflow, centred near ( $z/D_c = 2.3, r/D_c = 0.3$ ). The recirculation affects the spreading of the plume at the outer radial extent of the domain. Figure 9(b), which shows mean axial velocity component, is in accord with figure 7 in that at low elevations and low radii, there is a region where

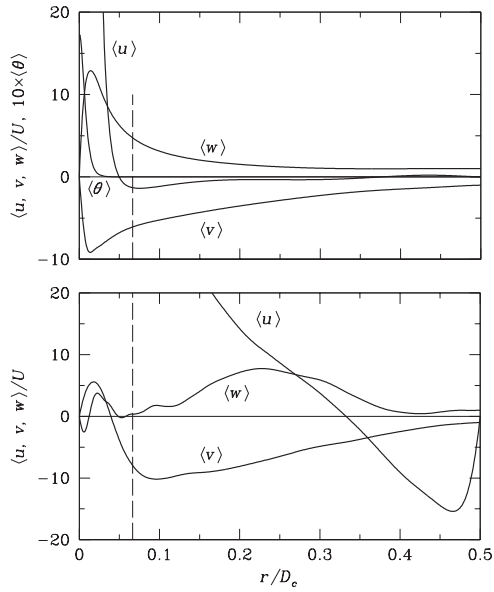


Figure 8: Mean flow profiles at (top)  $z/D_c = 0.1$ , (bottom)  $z/D_c = 0.9$ . Dashed vertical lines indicate minimum radius of experimental data collection, see figure 4.

the axial velocity and its radial extent are nearly independent of  $z$ . The distributions of axial–axial and axial–radial Reynolds stresses of figure 9 (c, d) show that turbulent diffusion/mixing of momentum is highest in very much the same locations where the dominance of buoyancy and swirl in the plume start to reduce. The azimuthal–axial Reynolds stress and azimuthal velocity–temperature covariance seen in figures 9 (e, f) show the strongest turbulent interactions between swirl and the plume of buoyancy occur at the lowest elevations where the whirl is still well organised. Finally, figure 9 (g) shows the mean swirl is highest in this same small region too, though there is also a much larger and diffuse region of swirl at about mid-elevation, associated with the recirculation zone seen in figure 9 (a).

## Conclusions

The experimental study described here shows that with a comparatively simple laboratory facility we are able to provide scaling results broadly in agreement with earlier studies of fire whirls. The key physical feature is that swirl tends to stabilise the whirl and reduce its spread rate below that for either a turbulent jet or turbulent buoyancy plume.

The numerical simulations have demonstrated the feasibility of using DNS for simulating swirling buoyant turbulent plumes, though in the results presented here there is only limited indication of fire whirl type behaviour near the lower end of the plume. Certainly the outcomes have emphasised the need to carefully characterise inflow boundary conditions if a good representation of experimental results is to be achieved. Current PIV measurements are aimed at providing these data, as well as velocity fields within the flame region. However, our results show the potential for the use of a combined experimental and DNS approach to help us achieve better understanding of the physical processes involved in fire whirls.

## References

[1] Battaglia, F., Rehm, R. G. and Baum, H. R., The fluid mechanics of fire whirls: An inviscid model, *Phys. Fluids*, **12**, 2000, 2859–2867.

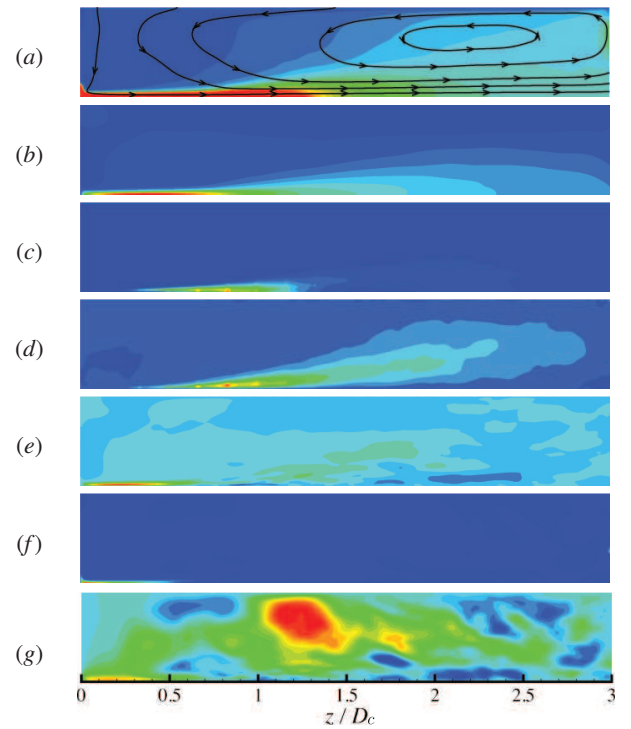


Figure 9: Contour maps of flow statistics. (a), mean temperature  $\langle\theta\rangle$  with streamlines computed from the time-average sectional velocity components, note recirculation zone; (b), mean axial velocity  $\langle u \rangle$ ; (c), axial velocity variance  $\langle u'u' \rangle$ ; (d), axial/radial Reynolds shear stress  $\langle u'v' \rangle$ ; (e), axial/azimuthal Reynolds shear stress  $\langle u'w' \rangle$ ; (f), fluctuating temperature/azimuthal velocity correlation  $\langle \theta'w' \rangle$ ; (g), mean azimuthal velocity  $\langle w \rangle$ .

[2] Blackburn, H. M. and Sherwin, S. J., Formulation of a Galerkin spectral element–Fourier method for three-dimensional incompressible flows in cylindrical geometries, *J. Comput. Phys.*, **197**, 2004, 759–778.

[3] Dong, S., Karniadakis, G. E. and Chrysosostomidis, C., A robust and accurate outflow boundary condition for incompressible flow simulations on severely-truncated unbounded domains, *J. Comput. Phys.*, **261**, 2014, 83–105.

[4] Jeong, J. and Hussain, F., On the identification of a vortex, *J. Fluid Mech.*, **285**, 1995, 69–94.

[5] Koal, K., Stiller, J. and Blackburn, H. M., Adapting the spectral vanishing viscosity method for large-eddy simulations in cylindrical configurations, *J. Comput. Phys.*, **231**, 2012, 3389–3405.

[6] Kuwana, K., Sekimoto, K., Saito, K. and Williams, F. A., Scaling fire whirls, *Fire Safety J.*, **43**, 2008, 252–257.

[7] Morton, B. R., The physics of fire whirls, in *Mass Fire Symposium*, Canberra, 1969, paper B1.

[8] Schlichting, H., *Boundary-Layer Theory*, McGraw-Hill, 1979, 7th edition.

[9] Scorer, R. S., *Environmental Aerodynamics*, Ellis Horwood, 1978.